

SnO/ β -Ga₂O₃ vertical *pn* heterojunction diodes

Melanie Budde,^{1,2} Daniel Splith,^{3,2} Piero Mazzolini,^{1,4} Abbes Tahraoui,¹ Johannes Feldl,¹ Manfred Ramsteiner,¹ Holger von Wenckstern,³ Marius Grundmann,³ and Oliver Bierwagen¹

¹*Paul-Drude-Institut für Festkörperelektronik, Leibniz-Institut im Forschungsverbund Berlin e.V., Hausvogteiplatz 5-7, 10117 Berlin, Germany*

²*Both authors contributed equally to this work.*

³*Universität Leipzig, Felix-Bloch-Institut für Festkörperphysik, Halbleiterphysik, Linnéstraße 5, 04103 Leipzig, Germany*

⁴*Present address: Department of Mathematical, Physical and Computer Sciences, University of Parma, Viale delle Scienze 7/A, 43124 Parma, Italy*

(Dated: February 28, 2022)

Vertical *pn* heterojunction diodes were prepared by plasma-assisted molecular beam epitaxy of unintentionally-doped *p*-type SnO layers with hole concentrations ranging from $p = 10^{18}$ to 10^{19} cm⁻³ on unintentionally-doped *n*-type β -Ga₂O₃(-201) substrates with an electron concentration of $n = 2.0 \times 10^{17}$ cm⁻³. The SnO layers consist of (001)-oriented grains without in-plane epitaxial relation to the substrate. After subsequent contact processing and mesa etching (which drastically reduced the reverse current spreading in the SnO layer and associated high leakage) electrical characterization by current-voltage and capacitance-voltage measurement was performed. The results reveal a type-I band alignment and junction transport by thermionic emission in forward bias. A rectification of 2×10^8 at ± 1 V, an ideality factor of 1.16, differential specific on-resistance of 3.9 m Ω cm², and built-in voltage of 0.96 V were determined. The *pn*-junction isolation prevented parallel conduction in the highly-conductive Ga₂O₃ substrate (sheet resistance $R_S \approx 3 \Omega$) during van-der-Pauw Hall measurements of the SnO layer on top ($R_S \approx 150$ k Ω , $p \approx 2.5 \times 10^{18}$ cm⁻³, Hall mobility ≈ 1 cm²/Vs). The measured maximum reverse breakdown voltage of the diodes was 66 V, corresponding to a peak breakdown field 2.2 MV/cm in the Ga₂O₃-depletion region. Higher breakdown voltages that are required in high-voltage devices could be achieved by reducing the donor concentration in the β -Ga₂O₃ to increase the depletion width as well as improving the contact geometry to reduce field crowding.

During the last decade transparent semiconducting oxides (TSOs) have become a widely investigated class of materials. Their transparency and wide band gaps are especially suitable for optoelectronic and power electronic applications. Most studied TSOs are *n*-type such as Ga₂O₃, In₂O₃ or SnO₂. Out of these, Ga₂O₃ with the thermodynamically stable monoclinic polymorph β -Ga₂O₃, is predicted to outperform GaN and SiC for high-voltage power electronics.¹⁻³ This advantage is related to its ultra-wide band gap of $E_g \approx 4.8$ eV providing a high break-down field of ≈ 8 MV/cm and a reasonably high electron mobility around 200 cm²/Vs giving rise to a sufficiently low on-resistance. In addition, the availability of large area (e.g., 2 and 4 inch wafers^{4,5}) bulk β -Ga₂O₃ single crystals provides the basis for low-defect β -Ga₂O₃ devices required for ultimate performance.⁵⁻⁸ Edge-termination to manage field crowding in high-voltage power electronic devices is ideally realized by *pn*-junctions.⁹ Since bipolar doping is not possible for most TSOs,¹⁰⁻¹² including β -Ga₂O₃,^{13,14} *n*-type TSOs need to be combined with suitable *p*-type TSOs to form *pn*-heterojunctions.¹⁵

The first Ga₂O₃-based, all-oxide *pn*-junction was reported in 2016 by Kokubun et al., combining a β -Ga₂O₃ single crystal with Li-doped NiO as a *p*-type material.¹⁶ In the following years *pn*-heterojunction followed with the *p*-type materials NiO,^{9,17-19} Cu₂O,²⁰ Ir₂O₃²¹ and ZnCo₂O₄.²² A comparison of the properties of some of these *pn*-heterojunction diodes can be found in Ref. 23. In the latest publication, Gong et al. achieved a rectifica-

tion ratio of the current I at the voltage $\pm V$ ($S_V = \frac{I(V)}{I(-V)}$) of $S_{3V} > 10^{10}$ and a breakdown voltage (V_b) of 1.86 kV, correlated with a maximum (E_m) electric breakdown field of about 3.5 MV/cm, for NiO/ β -Ga₂O₃ diodes having a type-II band alignment.⁹ For these devices an ideality factor (η) around 2 has been observed,⁹ whereas values close to 1 have been published, for example by Lu et al., but with only $S_V \approx 10^4$ for the same materials combination.¹⁹

β -Ga₂O₃(100)-based diodes with $\eta = 1.22$ and $S_V > 10^{10}$ have been reported by Du et al., using sputtered SnO_x Schottky electrodes. The layers are described as a combination of SnO and Sn (based on Raman and X-ray photoelectron spectroscopy measurements) whose resistance between two Ti contacts were determined. In fact, SnO is a *p*-type oxide with a two orders of magnitude higher hole mobility than NiO^{24,25} and $E_g \approx 0.7$ eV.²⁶ Addressing the metastability of SnO with respect to Sn and SnO₂ we have determined the growth window for the formation of stoichiometric SnO by plasma-assisted molecular beam epitaxy (MBE) in our previous study: SnO was grown by a controlled Sn/O-plasma flux ratio at temperatures $\leq 400^\circ\text{C}$, resulting in *p*-type conductivity with Hall hole concentrations (p_H) and Hall mobilities ranging from 10^{18} to 10^{19} cm⁻³ and 1 to 6.0 cm²/Vs, respectively. The phase was stable under rapid thermal annealing (RTA) in different atmospheres up 300°C and transformed into *n*-type Sn₃O₄ and SnO₂ at 400°C.²⁵

In this letter, we report the fabrication and characteristics of vertical *pn*-heterojunction diodes consisting

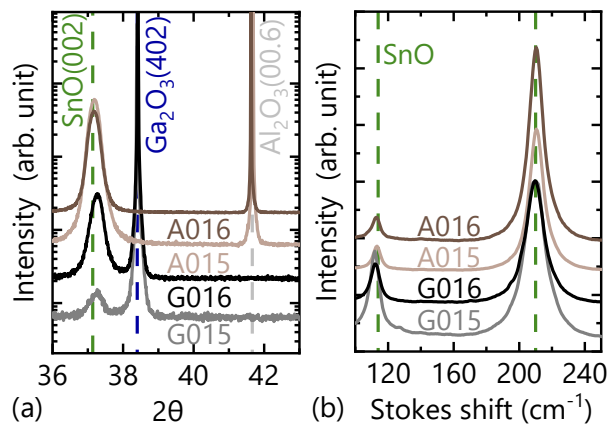


Figure 1. (a) XRD 2θ - ω scans and (b) bulk-sensitive Raman spectra of the reference samples A015 and A016, as well as the diodes G015 and G016. The Ga_2O_3 , Al_2O_3 , and SnO reflexes are indicated with blue, grey and green dashed lines, respectively, in (a), and the frequencies of optical phonon lines expected for SnO are indicated by dashed lines in (b).²⁵

of MBE-grown, p -type SnO layers on unintentionally n -type doped β - Ga_2O_3 ($\bar{2}01$) substrates grown by the edge-defined film-fed growth method (Tamura corporation).⁵ 5 mm \times 5 mm-large pieces diced from the β - Ga_2O_3 ($\bar{2}01$) substrate wafer were etched in phosphoric acid at 130 $^\circ\text{C}$ (removing $\simeq 500$ nm)²⁷ followed by an annealing step in oxygen (1 bar) at 950 $^\circ\text{C}$ for 1 hour in a tube furnace to remove a potentially present polishing-damage layer at the surface and to regain a stoichiometric Ga_2O_3 surface.^{28,29} A room-temperature Hall-measurement as described in Ref. 30 on a reference piece prepared the same way and from the same Ga_2O_3 wafer indicates an electron concentration (n) of $2.0 \times 10^{17} \text{ cm}^{-3}$, taking into account a Hall factor of 1.6.³¹ An ohmic contact was formed on the substrate backside by electron-beam evaporation of 20 nm Ti/100 nm Au and RTA for 1 minute at 470 $^\circ\text{C}$ in N_2 atmosphere³²⁻³⁴ before growth of the SnO layer to prevent its transformation into n -type SnO_x during RTA. After that the substrates were in-situ cleaned using an oxygen plasma [0.5 standard cubic centimeters per minute (sccm), 300 W] at a substrate heater temperature of 400 $^\circ\text{C}$ in the MBE growth chamber. Two samples (G015 and G016) were grown at 400 $^\circ\text{C}$ using oxygen fluxes of 0.15 sccm and 0.16 sccm, respectively. For both runs a plasma power of 300 W and a metallic Sn flux with a beam equivalent pressure of $1 \cdot 10^{-7}$ mbar and a growth time of 40 minutes were used. A piece of (insulating) c -plane Al_2O_3 was co-loaded in each run as a reference samples (A015, A016).

The results of symmetric, out-of-plane $2\theta - \omega$ X-ray diffraction (XRD) using Cu-K α radiation and bulk-sensitive Raman spectroscopy measurements using an excitation wavelength of 473 nm, as described in Ref. 25, are shown in Fig. 1 and confirm the presence of (001)-oriented SnO in all samples. In contrast to A015 and A016 with defined in-plane epitaxial relation²⁵, the

film of G016 shows a random rotational mosaicity as shown in the supplementary material.³⁵ In-situ thickness measurements using laser reflectometry³⁶ on the reference samples A015 and A016 indicate a total SnO thickness of 200 nm and 170 nm, respectively. Van-der-Pauw Hall measurements of the SnO layer of G016 using mesa-isolated (as described below) Greek-cross structures with Ti/Au top contacts (as described below) revealed $R_S \approx 150 \text{ k}\Omega$, $p \approx 2.5 \times 10^{18} \text{ cm}^{-3}$ (assuming a Hall scattering factor of 1.8),³⁷ and an in-plane Hall mobility $\mu_H \approx 1 \text{ cm}^2/\text{Vs}$. This result indicates a remarkable pn -junction isolation that prevented parallel conduction in the underlying highly-conductive Ga_2O_3 substrate (sheet resistance $R_S \approx 3 \Omega$) during the measurement of the SnO layer on top. In addition, we conducted Hall measurements in the van-der-Pauw geometry on the reference layers A015 and A016 for which we expected similar p to those of G015 and G016: A sheet resistance of 184 k Ω and 46 k Ω was extracted with $p=2.0 \times 10^{18} \text{ cm}^{-3}$ and $1.8 \times 10^{19} \text{ cm}^{-3}$ as well as $\mu_H=1.6$ and $0.8 \text{ cm}^2/\text{Vs}$ for A015 and A016, respectively. All measured hole concentrations are well below the critical value ($p_{\text{Mott}} \approx 9 \times 10^{19} \text{ cm}^{-3}$)²⁵ for the Mott transition; the hole mobilities are below those of single crystalline films due scattering from rotational-domain or grain boundaries in A015/A016,²⁵ or G016, respectively. In the following we assume the net donor and acceptor concentration N_D and N_A in the Ga_2O_3 and SnO to be equal to the measured n and p , respectively.

Square shaped 20 nm Ti/100 nm Au top contacts with sizes varying between $55 \times 55 \mu\text{m}^2$ and $180 \times 180 \mu\text{m}^2$ were defined on the grown SnO layer using a photolithography, electron-beam evaporation, and lift-off without additional RTA to prevent the transformation of the SnO layer into n -type SnO_x .²⁵ Notwithstanding, these contacts are ohmic with specific contact resistance of $\rho_c \approx 0.05 \text{ m}\Omega \text{ cm}^2$ on A015 and $\rho_c \approx 3.4 \text{ m}\Omega \text{ cm}^2$ on G016 as shown in the supplementary material.³⁵ After initial current-voltage (IV) measurements between top contacts and bottom contact, mesa etching of the SnO layer was performed on G015 and G016 to isolate the top contacts using a lithographically-defined resist mask and an inductively coupled plasma (ICP) inside a reactive ion etching system. A gas combination of 5 sccm Cl_2 and 20 sccm BCl_3 at a pressure of 1.3 Pa resulted in a suitable etch rate of about 45 nm/min at an ICP coil power of 100 W and a DC bias power of 25 W. Fig. 2 (a) schematically illustrates the cross-section of the resulting diode. A top-view micrograph of a $180 \times 180 \mu\text{m}^2$ contact pad after mesa etching (ME) is shown in Fig. 2 (b). Fig. 2 (c) shows typical room-temperature (RT) current-voltage (IV) characteristics of the two pn -junctions before and after mesa etching with voltage applied to the $180 \times 180 \mu\text{m}^2$ top contacts and the grounded bottom contact. In all cases rectification as expected for a pn -diode can be observed. Before mesa etching, however, a high reverse current is observed for both samples, resulting in a $S_{1V} \approx 100$. A drastic reduction of the reverse

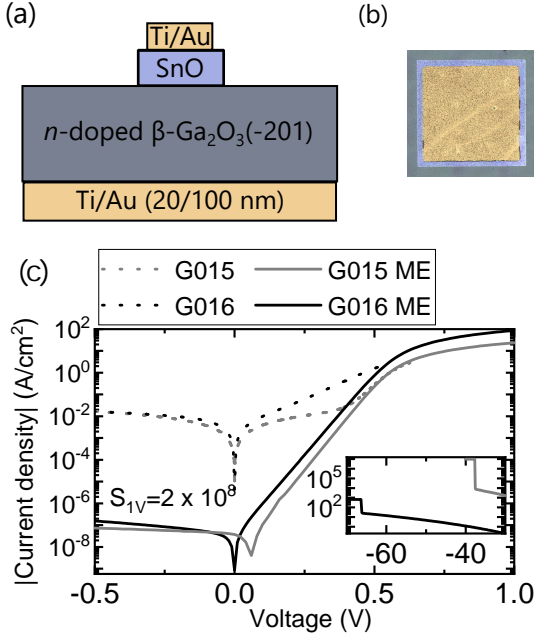


Figure 2. (a) Cross-section schematic of the vertical SnO/Ga₂O₃ heterojunction diodes after mesa etching (ME). (b) Micrograph showing a 180×180 μm² contact pad after ME. The mesa of the SnO thin film (light blue) is visible around the contact pad (gold). (c) Room-temperature *IV* curves of sample G015 and G016 measured on 180×180 μm² contacts in a semi-logarithmic plot before and after ME including the rectification factor S_V at 1 V. The inset shows the breakdown measurements after ME on one contact for each sample.

current was achieved by mesa etching, resulting in a significant increase of S_{1V} to 2×10^8 . This improvement can be explained by preventing the spreading of the reverse current in the SnO layer over the entire sample area as detailed in the supplementary information.³⁵ The inset of Fig. 2 (c) shows the breakdown behavior of G015 and G016. Breakdown voltages of -37 V and -66 V were measured on one contact of G015 and G016, respectively. The heterojunction *IV* characteristics in forward direction can be described by the Shockley equation:^{22,38}

$$I = I_S \left[\exp\left(\frac{qV - IR_s}{\eta k_B T}\right) - 1 \right] + \frac{V - IR_s}{R_p} + I_0. \quad (1)$$

Here, I_S is the saturation current, η the ideality factor, k_B the Boltzmann constant, q the elementary charge, T the absolute temperature, V the applied voltage, and R_s and R_p are the series and parallel resistance, respectively. In contrast to G016 ME, G015 ME shows a slight shift towards positive voltages. This shift is caused by a capacitive charging current during the voltage sweep which can be described by I_0 .³⁹ The modeled curves together with the measured data are shown in Fig. 3 for two diodes. In both cases η is close to unity, 1.06 and 1.16 for G015 ME and G016 ME, respectively, which indicates a high diode quality. The turn-on voltage was found to be between

0.50 V and 0.52 V by a linear fit of the forward bias (see inset of Fig 3). From the series resistance determined by the fit, the differential specific on-resistance was obtained to be 16.5 mΩ cm² and 3.9 mΩ cm² for G015 ME and G016 ME, respectively.

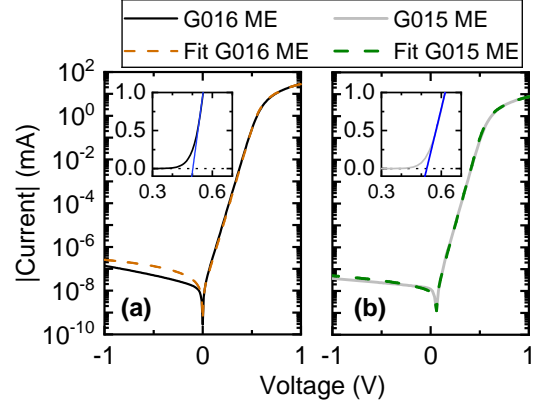


Figure 3. Room-temperature *IV* curves measured on 180 × 180 μm² contact pads after ME on the samples (a) G015 (grey) and (b) G016 (black) including the modeled curve (green and brown) using the Shockley equation. The inset shows the measurement of each sample in the linear plot together with the fit (blue) of the turn-on voltage.

Room-temperature capacitance-voltage (*CV*) measurements at 1 MHz are shown in Fig. 4(a) as $C^{-2} - V$ plot for both samples after ME. The capacitance of a *pn*-heterojunction is described by⁴¹

$$C = A_0 \left[\frac{q\epsilon_n\epsilon_p\epsilon_0 N_D N_A}{2(\epsilon_n N_D + \epsilon_p N_A)} \right]^{1/2} (V_{bi} - V - k_B T)^{-1/2}. \quad (2)$$

The relative dielectric constants of SnO, Ga₂O₃ and the permittivity of vacuum are ϵ_p , ϵ_n and ϵ_0 , respectively. V_{bi} , A_0 , N_D and N_A are the built-in potential, the area

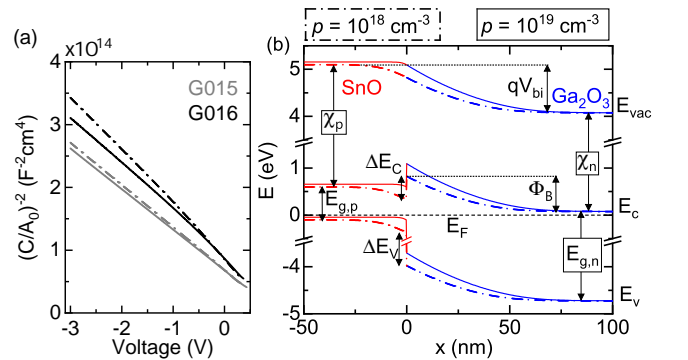


Figure 4. (a) Results of the *CV* measurements of two contacts on each, G015 and G016 represented by $(C/A_0)^{-2}(V)$ plot with contact area A_0 . (b) Estimated band diagram of the *p*-SnO/*n*-Ga₂O₃ junction using values from literature and the determined built-in potential. The diagram was calculated using the Open Band Parameters Device Simulator package.⁴⁰

of the junction, the net concentration of donors in Ga_2O_3 and that of acceptors in SnO , respectively. Dielectric constants ϵ_p and ϵ_n of 18.8 for SnO ⁴² and 10 for Ga_2O_3 ⁴³ were used. The built-in potential can be extracted by a linear extrapolation of C^{-2} to zero whose slope yields the effective net doping density $N_t = \frac{1}{\epsilon_t} \frac{\epsilon_n N_D \epsilon_p N_A}{\epsilon_n N_D + \epsilon_p N_A}$. Due to the significantly higher N_A of the SnO layer than N_D of the Ga_2O_3 substrate, the depletion region mainly develops inside the Ga_2O_3 whose properties are thus expected to dominate N_T : Assuming $\epsilon_t = \epsilon_n$ yields $N_t = (2.1 \pm 0.1) \times 10^{17} \text{ cm}^{-3}$, which is in good quantitative agreement with $n = 2.0 \times 10^{17} \text{ cm}^{-3}$ in the Ga_2O_3 . No significant differences can be seen for the values of the two samples so that we report the average value extracted from two measured diodes on each sample, resulting in $V_{bi} = 1.07 \pm 0.03 \text{ V}$. Using V_{bi} and known material parameters of Ga_2O_3 [band gap $E_{g,n} = 4.8 \text{ eV}$, electron affinity $\chi_n = 4.0 \text{ eV}$,⁴⁴ $\epsilon_n = 10$, density-of-states effective electron mass $m_{\text{eff},e} = 0.28 m_0$ ⁴⁵ (m_0 is the free electron mass)], and SnO (band gap $E_{g,p} = 0.7 \text{ eV}$,²⁶ $\epsilon_p = 18.8$, density-of-states effective hole mass $m_{\text{eff},h} = 1.7 m_0$ ⁴⁶), we can calculate an estimated band alignment diagram, shown in Fig 4(b) for $N_{D,n} = 2 \times 10^{17} \text{ cm}^{-3}$ and $N_{A,p} = 1 \times 10^{18} \text{ cm}^{-3}$ as well as $N_{A,p} = 1 \times 10^{19} \text{ cm}^{-3}$. The higher acceptor concentration changes the band diagram slightly (decrease of the band bending in the p -region, increase in the n -region) since the depletion at the heterointerface spreads predominantly to the substrate. In order to obtain a built-in potential of 1.1 V, it is necessary to assume an electron affinity of $\chi_p = 4.5 \text{ eV}$ for SnO . This value is in the same range as values reported in literature, which scatter from 3.59 eV to 5.1 eV.^{47–49}

The band alignment shown in Fig. 4(b) is a type-I alignment.¹⁵ Due to the small band-gap of SnO , the conduction band of SnO is below that of Ga_2O_3 . This renders thermionic emission as a possible transport mechanism for the diode; above the conduction band, thermally accessible states exist, similar to a Schottky barrier diode. Electrons injected from the Ga_2O_3 can either drift through the SnO to the Ohmic metal contact or recombine in the SnO . Temperature dependent IV -measurements between 50 K and 380 K verify thermionic emission as the dominating transport mechanism in forward direction: In Fig 5, an example of the resulting IV -characteristics for selected temperatures is shown. Similar characteristics were observed also for other contacts. By fitting with the Shockley equation, we determined I_S . For thermionic emission over a laterally homogeneous barrier $\log(I_S/T^2)$ is supposed to be linear with T^{-1} . Instead, we found a quadratic behavior for $T > 100 \text{ K}$ (see Fig. S6 in the supplementary material³⁵) which indicates thermionic emission over a Gaussian distributed lateral inhomogeneous barrier.⁵⁰ Therefore, the effective barrier height $\Phi_{B,\text{eff}}$ was calculated from the saturation current using

$$I_S = A_0 A^* \frac{m_{\text{eff},n}}{m_0} T^2 \exp\left(-\frac{\Phi_{B,\text{eff}}}{k_B T}\right),$$

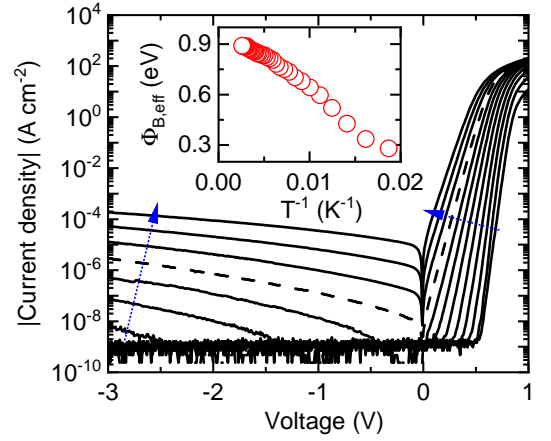


Figure 5. Temperature dependent IV -characteristics of one $\text{SnO}/\text{Ga}_2\text{O}_3$ contact for selected temperatures. The dashed line is the measurement at $T = 300 \text{ K}$, each characteristic has a temperature difference of about 30 K to its neighbors. At $|j| \approx 10^{-9} \text{ A cm}^{-2}$, the noise level of the measurement unit is reached. In the inset, a plot of the effective barrier height in dependence on T^{-1} is shown. Dotted arrows indicate the trend with increasing T .

where A^* is the Richardson constant. At $T = 300 \text{ K}$, a value of $\Phi_{B,\text{eff}} = 0.9 \text{ eV}$ was determined. By plotting $\Phi_{B,\text{eff}}$ vs. T^{-1} (see inset of Fig. 5) the mean barrier height $\bar{\Phi}_{B,0} = 1.02 \pm 0.04 \text{ eV}$ was determined as mean value of the linear extrapolation of $\Phi_{B,\text{eff}}$ to $T^{-1} = 0$ for four different contacts.⁵⁰ The good agreement between the mean barrier height and the built-in voltage corroborates the assumption of dominating thermionic emission. More details on the parameter extraction of the inhomogeneous barrier are given in the supplementary material.³⁵

In conclusion, we have demonstrated that SnO (with $p = 10^{18}$ to 10^{19} cm^{-3}) and $\beta\text{-Ga}_2\text{O}_3$ (with $n = 2 \times 10^{17} \text{ cm}^{-3}$) form a rectifying pn -heterojunction with a type-I band alignment and junction transport in forward bias by thermionic emission. A rectification of 2×10^8 at $\pm 1 \text{ V}$, ideality factor of 1.16, differential specific on-resistance of $3.9 \text{ m}\Omega \text{ cm}^2$, built-in voltage of 0.96 V, and reverse breakdown voltage of 66 V were achieved. From the band diagram, the depletion layer width $w_d = 610 \text{ nm}$ and maximum breakdown field $E_m = 2.2 \text{ MV/cm}$ were estimated at the breakdown voltage. This E_m is appreciable but well below the theoretical limit of Ga_2O_3 (8 MV/cm),¹ likely related to field spikes at the corners of the square shaped contacts as well as missing field plates. By reducing the donor concentration of the Ga_2O_3 (to increase the depletion layer thickness) and improving the contact geometry the breakdown voltage can be increased towards values required in high-voltage devices. For example, a donor concentration of $\approx 10^{16} \text{ cm}^{-3}$ while maintaining a comparably high p in the SnO to keep the (high-field) depletion region in the Ga_2O_3 could enable breakdown voltages of $\approx 1 \text{ kV}$.²³

ACKNOWLEDGMENTS

We would like to thank H.-P. Schönherr, C. Stemmler and K. Morgenroth for MBE support, S. Rauwerdink, W. Anders, and W. Seidel for sample processing, and Y. Takagaki for critically reading the manuscript. This work was performed in the framework of GraFOx, a Leibniz-ScienceCampus partially funded by the Leibniz association. M.B. and J.F. gratefully acknowledge financial support by the Leibniz association. D.S., H.v.W, and M.G. acknowledge funding from the European Social Fund within the Young Investigator Group “Oxide Heterostructures” (SAB 100310460) as well as support by Universität Leipzig within the research profile area “Complex matter”.

DATA AVAILABILITY

The data that support the findings of this study are available from the corresponding author upon reasonable request.

REFERENCES

- ¹M. Higashiwaki, K. Sasaki, A. Kuramata, T. Masui, and S. Yamakoshi, *Appl. Phys. Lett.*, **100**(1), 013504 (2012). doi:10.1063/1.3674287.
- ²S. J. Pearton, J. Yang, P. H. Cary, F. Ren, J. Kim, M. J. Tadjer, and M. A. Mastro, *Applied Physics Reviews*, **5**(1), 011301 (2018). doi:10.1063/1.5006941.
- ³Z. Galazka, *Semiconductor Science and Technology*, **33**(11), 113001 (2018). doi:10.1088/1361-6641/aadf78. URL <https://doi.org/10.1088/1361-6641/aadf78>.
- ⁴Z. Galazka, K. Irmscher, R. Uecker, R. Bertram, M. Pietsch, A. Kwasniewski, M. Naumann, T. Schulz, R. Schewski, D. Klimm, and M. Bickermann, *Journal of Crystal Growth*, **404**(0), 184 – 191 (2014). ISSN 0022-0248. doi:10.1016/j.jcrysgro.2014.07.021. URL <https://doi.org/10.1016/j.jcrysgro.2014.07.021>.
- ⁵A. Kuramata, K. Koshi, S. Watanabe, Y. Yamaoka, T. Masui, and S. Yamakoshi, *Jpn. J. Appl. Phys.*, **55**(12), 1202A2 (2016). doi:10.7567/jjap.55.1202a2.
- ⁶N. Ueda, H. Hosono, R. Waseda, and H. Kawazoe, *Appl. Phys. Lett.*, **70**(26), 3561–3563 (1997). doi:10.1063/1.119233.
- ⁷Z. Galazka, R. Uecker, K. Irmscher, M. Albrecht, D. Klimm, M. Pietsch, M. Bruetzsch, R. Bertram, S. Ganschow, and R. Fornari, *CRYSTAL RESEARCH AND TECHNOLOGY*, **45**(12, Sp. Iss. SI), 1229–1236 (2010). ISSN 0232-1300. doi:10.1002/crat.201000341.
- ⁸Z. Galazka, R. Uecker, D. Klimm, K. Irmscher, M. Naumann, M. Pietsch, A. Kwasniewski, R. Bertram, S. Ganschow, and M. Bickermann, *ECS Journal of Solid State Science and Technology*, **6**(2), Q3007–Q3011 (2016). doi:10.1149/2.0021702jss.
- ⁹H. H. Gong, X. H. Chen, Y. Xu, F.-F. Ren, S. L. Gu, and J. D. Ye, *Appl. Phys. Lett.*, **117**(2), 022104 (2020). doi:10.1063/5.0010052.
- ¹⁰S. Lany, J. Osorio-Guillén, and A. Zunger, *Phys. Rev. B*, **75**(24), 241203 (2007). doi:10.1103/PhysRevB.75.241203.
- ¹¹J. Robertson and S. Clark, *Phys. Rev. B*, **83**(7), 075205 (2011). doi:10.1103/PhysRevB.83.075205.
- ¹²S. Lany and A. Zunger, *Physical Review B*, **80**(8), 085202 (2009). doi:10.1103/PhysRevB.80.085202. URL <http://link.aps.org/doi/10.1103/PhysRevB.80.085202>.
- ¹³J. B. Varley, A. Janotti, C. Franchini, and C. G. Van de Walle, *Phys. Rev. B*, **85**, 081109 (2012). doi:10.1103/PhysRevB.85.081109. URL <http://link.aps.org/doi/10.1103/PhysRevB.85.081109>.
- ¹⁴A. Kyrtsos, M. Matsubara, and E. Bellotti, *Applied Physics Letters*, **112**(3), 032108 (2018). doi:10.1063/1.5009423.
- ¹⁵M. Grundmann, F. Klüpfel, R. Karsthof, P. Schlupp, F.-L. Schein, D. Splith, C. Yang, S. Bitter, and H. von Wenckstern, *Journal of Physics D: Applied Physics*, **49**(21), 213001 (2016). doi:10.1088/0022-3727/49/21/213001.
- ¹⁶Y. Kokubun, S. Kubo, and S. Nakagomi, *Appl. Phys. Express*, **9**, 091101 (2016). doi:10.7567/APEX.9.091101.
- ¹⁷M. I. Pintor-Monroy, D. Barrera, B. L. Murillo-Borjas, F. J. Ochoa-Estrella, J. W. P. Hsu, and M. A. Quevedo-Lopez, *ACS Appl. Mater. Inter.*, **10**(44), 38159–38165 (2018). doi:10.1021/acsami.8b08095.
- ¹⁸K.-H. Li, N. Alfaraj, C. H. Kang, L. Braic, M. N. Hedhili, Z. Guo, T. K. Ng, and B. S. Ooi, *ACS Appl. Mater. Inter.*, **11**(38), 35095–35104 (2019). doi:10.1021/acsami.9b10626.
- ¹⁹X. Lu, X. Zhou, H. Jiang, K. W. Ng, Z. Chen, Y. Pei, K. M. Lau, and G. Wang, *IEEE Electron Device Lett.*, **41**(3), 449–452 (2020). doi:10.1109/led.2020.2967418.
- ²⁰T. Watahiki, Y. Yuda, A. Furukawa, M. Yamamuka, Y. Takiguchi, and S. Miyajima, *Appl. Phys. Lett.*, **111**(22), 222104 (2017). doi:10.1063/1.4998311.
- ²¹S. Kan, S. Takemoto, K. Kaneko, I. Takahashi, M. Sugimoto, T. Shinohe, and S. Fujita, *Appl. Phys. Lett.*, **113**(21), 212104 (2018). doi:10.1063/1.5054054.
- ²²P. Schlupp, D. Splith, H. von Wenckstern, and M. Grundmann, *Phys. Status Solidi A*, **216**(7), 1800729 (2019). doi:10.1002/pssa.201800729.
- ²³D. Splith, P. Schlupp, H. von Wenckstern, and M. Grundmann. Diodes 2. In *Gallium Oxide*, pages 689–702. Springer International Publishing, (2020). doi:10.1007/978-3-030-37153-1_37.
- ²⁴J.-Y. Zhang, W. Li, R. L. Z. Hoye, J. MacManus-Driscoll, M. Budde, O. Bierwagen, L. Wang, Y. Du, M. Wahila, L. F. J. Piper, T.-L. Lee, H. Edwards, V. R. Dhanak, and H. Zhang, *J. Mater. Chem. C*, **6**, 2275–2282 (2018). doi:10.1039/C7TC05331B.
- ²⁵M. Budde, P. Mazzolini, J. Feldl, C. Golz, T. Nagata, S. Ueda, G. Hoffmann, M. Ramsteiner, and O. Bierwagen.
- ²⁶Y. Ogo, H. Hiramatsu, K. Nomura, H. Yanagi, T. Kamiya, M. Hirano, and H. Hosono, *Applied Physics Letters*, **93**(3), 032113 (2008). doi:10.1063/1.2964197.
- ²⁷T. Oshima, T. Okuno, N. Arai, Y. Kobayashi, and S. Fujita, *Jpn. J. Appl. Phys.*, **48**(4), 040208 (2009). doi:10.1143/jjap.48.040208. URL <https://doi.org/10.1143/jjap.48.040208>.
- ²⁸P. Mazzolini, P. Vogt, R. Schewski, C. Wouters, M. Albrecht, and O. Bierwagen, *APL Materials*, **7**(2), 022511 (2019). doi:10.1063/1.5054386. URL <https://doi.org/10.1063/1.5054386>.
- ²⁹P. Mazzolini, A. Falkenstein, C. Wouters, R. Schewski, T. Markurt, Z. Galazka, M. Martin, M. Albrecht, and O. Bierwagen, *APL Materials*, **8**(1), 011107 (2020). doi:10.1063/1.5135772.
- ³⁰C. Golz, Z. Galazka, J. Lähnemann, V. Hortelano, F. Hatami, W. T. Masselink, and O. Bierwagen, *Physical Review Materials*, **3**(12), 124604 (2019). doi:10.1103/physrevmaterials.3.124604.
- ³¹N. Ma, N. Tanen, A. Verma, Z. Guo, T. Luo, H. G. Xing, and D. Jena, *Applied Physics Letters*, **109**(21), 212101 (2016). doi:http://dx.doi.org/10.1063/1.4968550. URL <http://scitation.aip.org/content/aip/journal/apl/109/21/10.1063/1.4968550>.
- ³²M. Higashiwaki, K. Sasaki, T. Kamimura, M. Hoi Wong, D. Krishnamurthy, A. Kuramata, T. Masui, and S. Yamakoshi, *Appl. Phys. Lett.*, **103**(12), 123511 (2013). doi:10.1063/1.4821858. URL <https://doi.org/10.1063/1.4821858>.
- ³³Y. Yao, R. F. Davis, and L. M. Porter, *J. Electron. Mater.*, **46**(4), 2053 (2017). doi:10.1007/s11664-016-5121-1.
- ³⁴M.-H. Lee and R. L. Peterson, *APL Materials*, **7**(2), 022524 (2019). doi:10.1063/1.5054624. URL <https://doi.org/10.1063/1.5054624>.
- ³⁵Supplementary information.
- ³⁶P. Vogt and O. Bierwagen, *Appl. Phys. Lett.*, **106**(8), 081910 (2015). doi:10.1063/1.4913447. URL <https://doi.org/10.1063/1.4913447>.

- 1.4913447.
- ³⁷Y. Hu, J. Hwang, Y. Lee, P. Conlin, D. G. Schlom, S. Datta, and K. Cho, *Journal of Applied Physics*, **126**(18), 185701 (2019). doi:10.1063/1.5109265.
- ³⁸W. Shockley, *Bell System Technical Journal*, **28**(3), 435–489 (1949). doi:10.1002/j.1538-7305.1949.tb03645.x.
- ³⁹D. Splith, S. Müller, H. von Wenckstern, and M. Grundmann. Modeling of schottky barrier diode characteristics on heteroepitaxial beta-gallium oxide thin films. In F. H. Teherani, D. C. Look, and D. J. Rogers, editors, *Oxide-based Materials and Devices IX*. SPIE, (2018). doi:10.1117/12.2301370.
- ⁴⁰Open band parameter device simulator (obpds) package for python. URL <https://pypi.org/project/obpds/>.
- ⁴¹J. Donnelly and A. Milnes, *IEEE Transactions on Electron Devices*, **14**(2), 63–68 (1967). doi:10.1109/t-ed.1967.15900.
- ⁴²X. Li, L. Liang, H. Cao, R. Qin, H. Zhang, J. Gao, and F. Zhuge, *Appl. Phys. Lett.*, **106**(13), 132102 (2015). doi:10.1063/1.4916664. URL <https://doi.org/10.1063/1.4916664>.
- ⁴³A. Fiedler, R. Schewski, Z. Galazka, and K. Irmscher, *ECS Journal of Solid State Science and Technology*, **8**(7), Q3083–Q3085 (2019). doi:10.1149/2.0201907jss. URL <http://jss.ecsdl.org/content/8/7/Q3083.abstract>.
- ⁴⁴M. Mohamed, K. Irmscher, C. Janowitz, Z. Galazka, R. Manzke, and R. Fornari, *Applied Physics Letters*, 101(13), 132106 (2012). doi:10.1063/1.4755770. URL <http://link.aip.org/link/?APL/101/132106/1>.
- ⁴⁵S. Knight, A. Mock, R. Korlacki, V. Darakchieva, B. Monemar, Y. Kumagai, K. Goto, M. Higashiwaki, and M. Schubert, *Applied Physics Letters*, **112**(1), 012103 (2018). doi:10.1063/1.5011192. URL <https://doi.org/10.1063/1.5011192>.
- ⁴⁶J. B. Varley, A. Schleife, A. Janotti, and C. G. Van de Walle, *Applied Physics Letters*, 103(8), 082118 (2013). doi: <http://dx.doi.org/10.1063/1.4819068>. URL <http://scitation.aip.org/content/aip/journal/apl/103/8/10.1063/1.4819068>.
- ⁴⁷Y. Xu and M. A. Schoonen, *American Mineralogist*, **85**(3–4), 543–556 (2000). doi:10.2138/am-2000-0416.
- ⁴⁸X. Li, L. Liang, H. Cao, R. Qin, H. Zhang, J. Gao, and F. Zhuge, *Applied Physics Letters*, **106**(13), 132102 (2015). doi:10.1063/1.4916664.
- ⁴⁹Y. Ogo, H. Hiramatsu, K. Nomura, H. Yanagi, T. Kamiya, M. Kimura, M. Hirano, and H. Hosono, *physica status solidi (a)*, **206**(9), 2187–2191 (2009). doi:10.1002/pssa.200881792.
- ⁵⁰J. H. Werner and H. H. Güttler, *Journal of Applied Physics*, **69**(3), 1522–1533 (1991). doi:10.1063/1.347243.

Supplementary Material to —

SnO/ β -Ga₂O₃ vertical $p - n$ heterojunction diodes

Melanie Budde,^{1,2} Daniel Splith,^{3,2} Piero Mazzolini,^{1,4} Abbas Tahraoui,¹ Johannes Feldl,¹ Manfred Ramsteiner,¹ Holger von Wenckstern,³ Marius Grundmann,³ and Oliver Bierwagen¹

¹*Paul-Drude-Institut für Festkörperelektronik, Leibniz-Institut im Forschungsverbund Berlin e.V., Hausvogteiplatz 5-7, 10117 Berlin, Germany*

²*Both authors contributed equally to this work.*

³*Universität Leipzig, Felix-Bloch-Institut für Festkörperphysik, Halbleiterphysik, Linnéstraße 5, 04103 Leipzig, Germany*

⁴*Present address: Department of Mathematical, Physical and Computer Sciences, University of Parma, Viale delle Scienze 7/A, 43124 Parma, Italy*

(Dated: February 28, 2022)

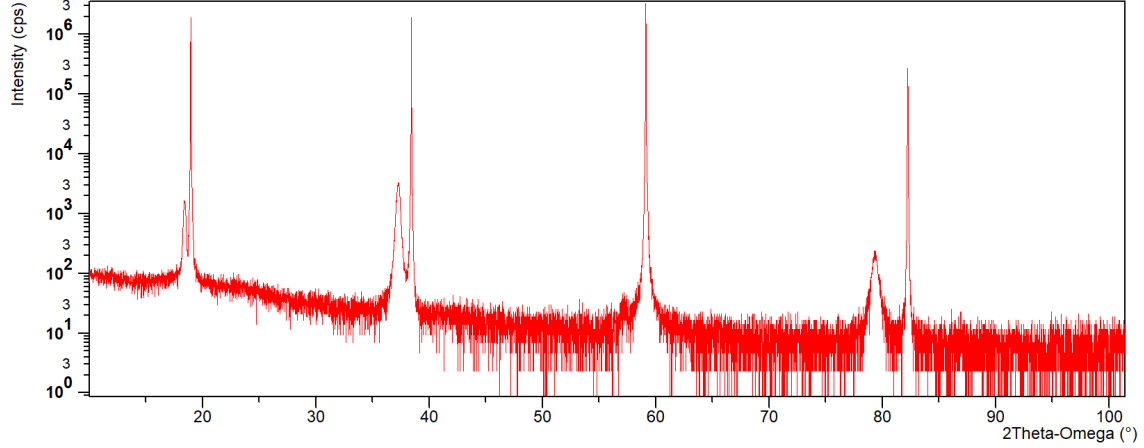


Figure S1. XRD wide-range out-of-plane symmetric $2\Theta - \omega$ scan of sample G016.

XRD ANALYSIS OF THE SNO FILM ON β -GA₂O₃(-201) IN SAMPLE G016

A wide-range out-of-plane symmetric $2\Theta - \omega$ scan of G016 shown in Fig. S1 indicates the presence of different orders of the β -Ga₂O₃-201 reflex (sharp, strong reflexes) accompanied on the left hand side by different orders of the SnO 002 reflex (weaker and wider). These results confirm the presence of out-of-plane 001 oriented SnO. Texture maps, shown in Fig. S2, of the 002 and 101 reflex of SnO were measured on G016 as well as a β -Ga₂O₃(-201) substrate for reference. The map of the SnO 002 reflex shown in Fig. S2(a) confirms the out-of-plane 001 orientation of the SnO film by the strong intensity of surface parallel SnO(001) planes (at $\chi = 0^\circ$). The additional intensity visible at (at $\chi \approx 80^\circ, \phi \approx 80^\circ$) is also present in the texture map on a β -Ga₂O₃(-201) substrate without grown SnO film (Fig. S2(b)) and is thus not related to the SnO film.

The in-plane orientation of the SnO film can be seen in the texture map of the SnO 101 reflex shown in Fig. S2(c). The same type of map for the β -Ga₂O₃(-201) substrate without grown SnO film is shown in Fig. S2(d) for reference. Again, reflexes related to the substrate are visible in G016. At $\chi \approx 52^\circ$, the tilt angle of the SnO 101 plane with respect to the 001 plane, a weak ring shaped pattern is visible indicating a polycrystalline SnO layer with randomly rotated but 001 out-of-plane oriented grains. The ω -rocking curve of the SnO 002 reflex, shown in Fig. S3, exhibits a full-width-at-half-maximum of 2.7° , indicative of the tilt mosaic of the out-of-plane orientation.

Thus, the SnO film consists of 001 oriented grains without any in-plane epitaxial relation to the β -Ga₂O₃(-201) substrate.

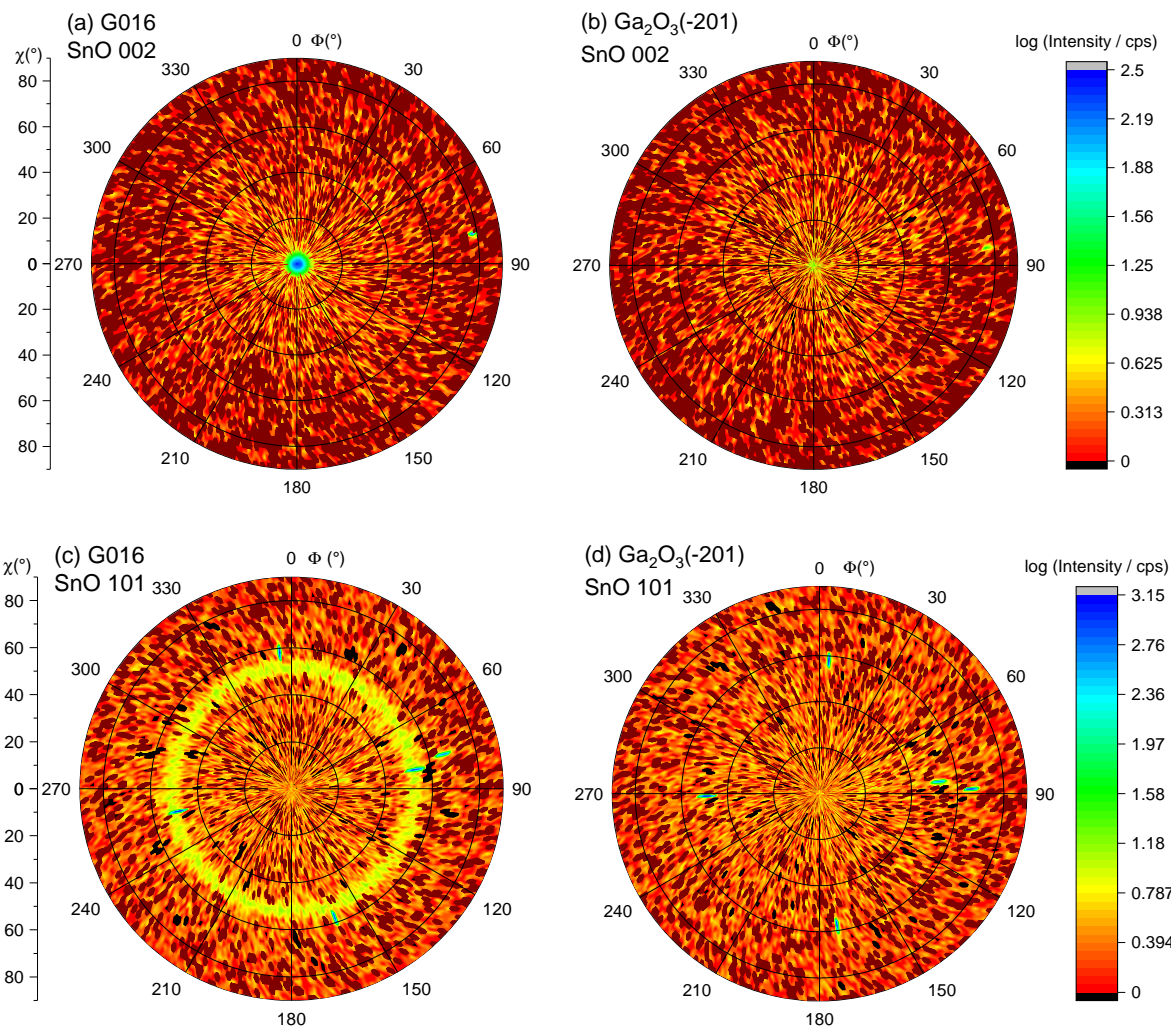


Figure S2. XRD texture maps of the SnO 002 (a,b) and SnO 101 (c,d) reflex measured on sample G016 (a, c) and a Ga₂O₃(-201) substrate (b, d) as reference.

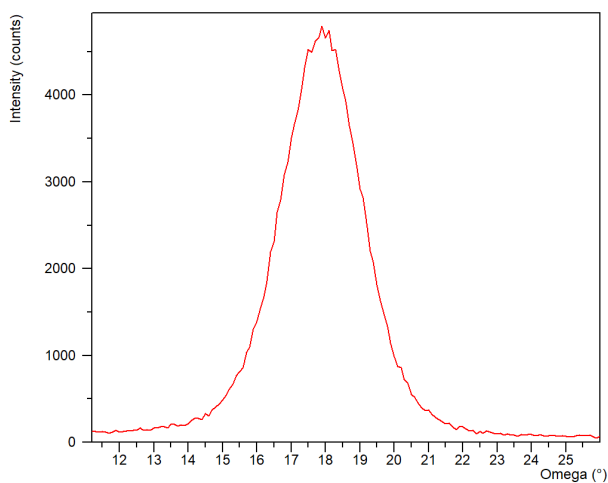


Figure S3. XRD ω -rocking curve of the SnO 002 reflex in sample G016.

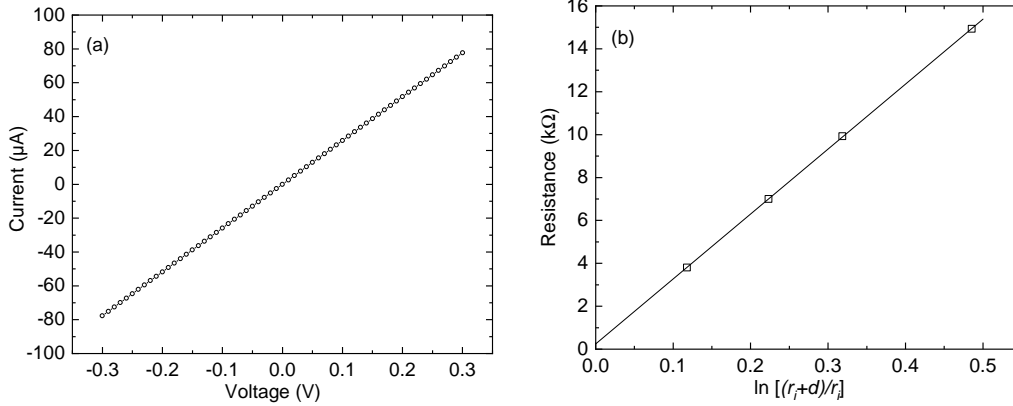


Figure S4. Characterization of Ti/Au contacts on p -SnO in sample A015 using cTLM patterns. (a) Current-voltage characteristics of the pattern with lowest spacing ($5 \mu\text{m}$) confirming an ohmic contact to the SnO. The extracted total resistance of $3.8 \text{ k}\Omega$ and those from other gap spacings are used in the analysis in (b), which reveals a sheet resistance (derived from the slope) of $190 \text{ k}\Omega$ and specific contact resistance of $\approx 0.05 \text{ m}\Omega \text{ cm}^2$.

OHMIC TI/AU CONTACTS TO p -TYPE SNO ON SAMPLES A015 AND G016

To assess the Ti/Au contact to p -type SnO, used as top contact in the diodes, we processed circular TLM (cTLM)² patterns with inner disc radius of $r_i = 80 \mu\text{m}$ and gap spacings ranging from $d = 5$ to $100 \mu\text{m}$ on samples A015 and G016 using the identical processing scheme to the top contacts of the diodes (photolithography, electron-beam evaporation, lift-off, no contact annealing). An optical micrograph of the cTLM structure (on a SnO_2 layer) can be found in Ref. 1. Current-voltage curves of the cTLM structures were linear as shown exemplarily for the pattern with the lowest gap spacing, i.e., the one with strongest contribution from the contact, of A015 in Fig. S4(a) and shown for all measured gap spacings of G016 in Fig. S5(right). This result confirms an ohmic contact between Ti and the p -type SnO of both samples. More importantly, the good linearity on G016 indicates negligible leakage of the current across the (rectifying) pn -junction. Analysis of the measured resistances as function of gap spacing, shown in Fig. S4(b) and Fig. S5(left), reveals a sheet resistance of $190 \text{ k}\Omega$ for A015 and $173 \text{ k}\Omega$ for G016, both in excellent agreement with the values extracted from the van-der-Pauw measurements. The extracted specific contact resistance is $\rho_c = 0.05 \text{ m}\Omega \text{ cm}^2$ and $\rho_c = 3.4 \text{ m}\Omega \text{ cm}^2$ for A015 and G016, respectively.

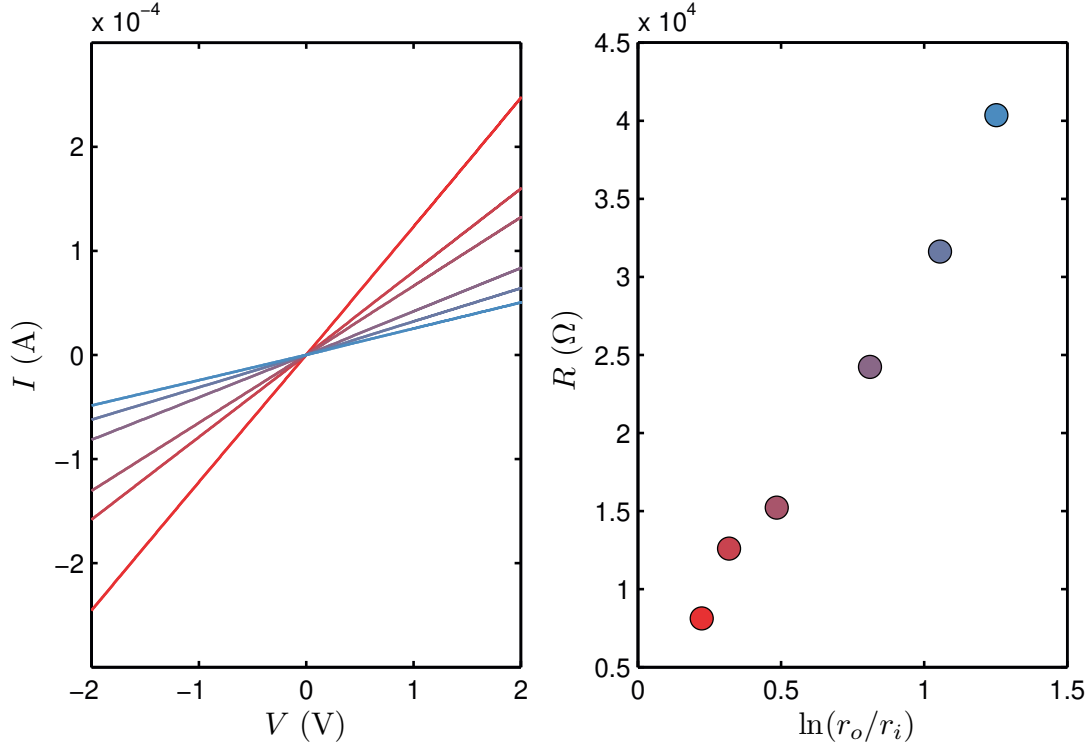


Figure S5. Characterization of Ti/Au contacts on p -SnO in sample G016 using cTLM patterns. (left) Current-voltage characteristics of the patterns confirming an ohmic contact to the SnO and negligible current leakage into the underlying Ga_2O_3 . (right) The extracted total resistance of from the different gap spacings are used in the analysis to obtain a sheet resistance (derived from the slope) of $173\text{ k}\Omega$ and specific contact resistance of $\approx 3.4\text{ m}\Omega\text{ cm}^2$.

REVERSE LEAKAGE ON G015 AND G016 IN ABSENCE OF MESA ISOLATION

Without mesa etching current can laterally spread from the top contact pad in the SnO layer (with sheet resistance for lateral transport on the order of $100\text{ k}\Omega$) if it helps minimizing the total resistance to the back-contact on the Ga_2O_3 substrate. In forward bias, vertical current flow from the p -type SnO into n -type Ga_2O_3 can take place and the measured series resistance on the order or $10\text{--}100\ \Omega$ is well below the sheet resistance of the SnO layer, making current spreading not favorable. This scenario changes drastically in reverse bias where current flow across the pn -junction is impeded and current spreading in the SnO helps maximizing the active junction area (or allowing the current to flow through isolated leakage spots) and thus total current flow across the pn -junction. From a linear fit of the reverse

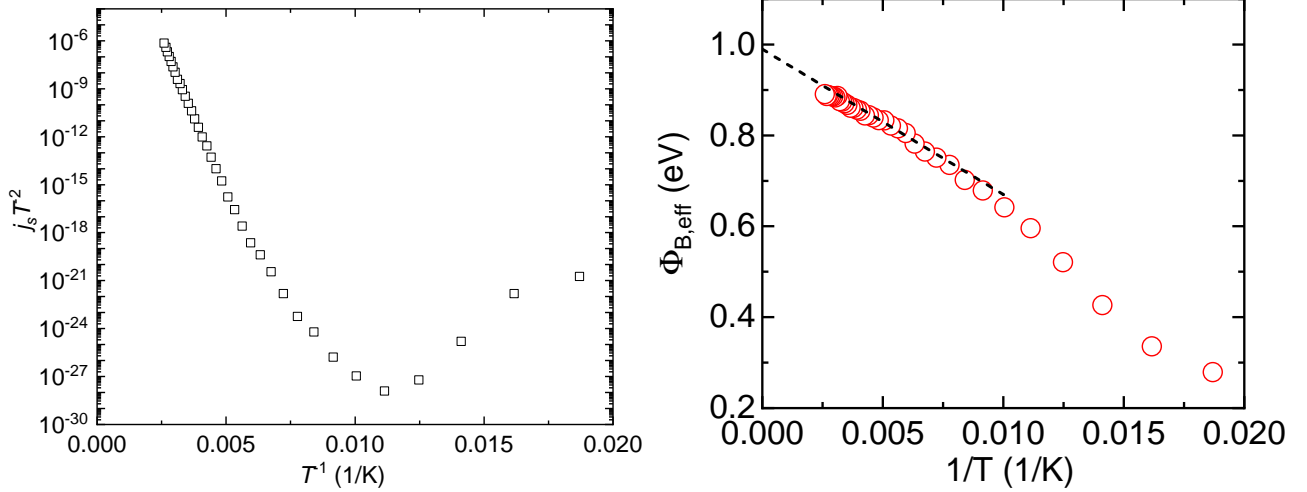


Figure S6. left: Representative temperature dependence of the saturation current: $\log(I_S/T^2)$ vs. T^{-1} of a diode on sample G016.

right: Representative linear fit of the effective barrier height Φ_B^{eff} to obtain the mean barrier height $\bar{\Phi}_{B,0}$ and the standard deviation of its distribution σ_0 .

current in the diodes prior to mesa etching a parallel leakage resistance on the order of $80 \text{ k}\Omega$ was extracted, which is on the order of the SnO sheet resistance, strongly suggesting current spreading to limit the reverse leakage current.

Two successive mesa etchings of G016 to total etch depths of 140 and 180 nm were performed with significant reduction of the reverse leakage only at 180 nm. Consequently, current spreading still took place after the 140 nm-etch and thus, the SnO layer thickness on G016 is between 140 and 180 nm, in good agreement with the SnO film thickness of 170 nm on the reference sample A016.

ANALYSIS OF Laterally Inhomogeneous Barriers

The quadratic behavior $\log(I_S/T^2)$ vs. T^{-1} shown in Fig. S6(left) indicates thermionic emission over a Gaussian distributed lateral inhomogeneous barrier being the dominant transport mechanism.⁵ This type of barrier can be characterized by the mean barrier height $\bar{\Phi}_{B,0} = 1.02 \pm 0.04 \text{ eV}$ and the standard deviation of its distribution $\sigma_0 = 0.080 \pm 0.008 \text{ eV}$, which were extracted from the temperature dependence according to $\Phi_B^{\text{eff}} = \bar{\Phi}_{B,0} - \frac{\sigma_0^2}{2k_B T}$.⁵ Note that the values given here and in the following are the mean values of IVT -measurements on four different contacts. Further, from a linear fit of $\eta^{-1} - 1$ vs. T^{-1} (not shown) we determined the voltage coefficients ρ_2 and ρ_3 of $\bar{\Phi}_{B,0}$ and σ_0 to be

-0.15 ± 0.04 and -0.009 ± 0.003 eV, respectively. Alternatively, the homogeneous barrier height can be extracted from the empiric model of Schmitsdorf and Mönch^{3,4} by linear extrapolation of $\Phi_{B,\text{eff}}$ vs. η to $\eta = 1.01$. The resulting homogeneous barrier height of 0.96 ± 0.04 eV is again in good agreement with the built-in voltage $V_{bi} = 1.07 \pm 0.03$ V as well as the mean barrier height.

REFERENCES

- ¹Oliver Bierwagen, Mark E. White, Min-Ying Tsai, Takahiro Nagata, and James S. Speck. Non-alloyed schottky and ohmic contacts to as-grown and oxygen-plasma treated n-type SnO_2 (110) and (101) thin films. *Applied Physics Express*, 2(10):106502, 2009. doi: 10.1143/APEX.2.106502. URL <http://apex.ipap.jp/link?APEX/2/106502/>.
- ²G. K. Reeves. Specific contact resistance using a circular transmission line model. *Solid-State Electronics*, 23(5):487–490, May 1980. doi:10.1016/0038-1101(80)90086-6.
- ³R. F. Schmitsdorf. Explanation of the linear correlation between barrier heights and ideality factors of real metal-semiconductor contacts by laterally nonuniform schottky barriers. *Journal of Vacuum Science & Technology B: Microelectronics and Nanometer Structures*, 15(4):1221, jul 1997. doi:10.1116/1.589442.
- ⁴R.F. Schmitsdorf and W. Mönch. Influence of the interface structure on the barrier height of homogeneous schottky contacts. *The European Physical Journal B*, 7(3):457–466, feb 1999. doi:10.1007/s100510050634.
- ⁵J. H. Werner and H. H. Güttler. Barrier inhomogeneities at schottky contacts. *Journal of Applied Physics*, 69(3):1522–1533, feb 1991. doi:10.1063/1.347243.